



# Hierarchical photocatalyst of $\text{In}_2\text{S}_3$ on exfoliated $\text{MoS}_2$ nanosheets for enhanced visible-light-driven Aza-Henry reaction

Zhen Li, Zhou Zhou, Jingwen Ma, Yang Li, Wenchao Peng, Guoliang Zhang, Fengbao Zhang, Xiaobin Fan\*

School of Chemical Engineering and Technology, State Key Laboratory of Chemical Engineering, Collaborative Innovation Center of Chemical Science and Engineering, Tianjin University, Tianjin 300354, China

## ARTICLE INFO

### Keywords:

Photocatalysis  
 $\text{In}_2\text{S}_3$   
 $\text{MoS}_2$   
Hierarchical heterostructure  
Organic synthesis

## ABSTRACT

Exploration of appropriate photocatalysts for visible-light-driven organic synthesis is of great importance. Here we design and construct a two-dimensional hierarchical  $\text{In}_2\text{S}_3/\text{MoS}_2$  composite as an excellent and reusable photocatalyst for Aza-Henry reaction. The dahlia-flower-like  $\text{In}_2\text{S}_3$  nanostructures are homogeneously grown on both sides of the two-dimensional  $\text{MoS}_2$  nanosheets via a hydrothermal reaction. The as-prepared two-dimensional hierarchical  $\text{In}_2\text{S}_3/\text{MoS}_2$  composite exhibits higher photocatalytic performance than pure  $\text{In}_2\text{S}_3$ . The hierarchical heterostructure can enhance the light absorption in the visible region, facilitate the separation of the photo-induced electron-hole pairs, offer rich active sites for photoredox reactions and promote the generation and migration of the  $\cdot\text{O}_2^-$  and  $\text{h}^+$ . Profiting from these compositional and structural features, the two-dimensional hierarchical  $\text{In}_2\text{S}_3/\text{MoS}_2$  composite shows remarkably enhanced photocatalytic performance and good stability.

## 1. Introduction

Visible-light-driven photocatalysis has sparked increasing interests in organic synthesis chemistry, on account of that visible light occupies the major part of the sunlight, which is regarded as an abundant, green and sustainable energy resource [1–3]. Developing appropriate photoredox catalysts, with the capacity to efficiently absorb the photons in the visible region, plays a dominating role in visible-light-driven organic synthesis [4]. Homogenous photocatalysts, like organic dyes [5,6] and transition metal complexes [7–9], have been widely used in photocatalytic organic synthesis. Nevertheless, their high cost, potential toxicity and poor reusability greatly impede their practical applications on a large scale. To reduce the cost and contamination, many heterogeneous photoredox catalysts have been fabricated, owing to their good recover ability and economical efficiency [10–17]. Among them, Indium sulfide ( $\text{In}_2\text{S}_3$ ), in particular the  $\beta\text{-In}_2\text{S}_3$ , is an attractive candidate, which is an n-type semiconductor with a narrow band gap (2.0–2.3 eV). It is of great potential to be used in photocatalytic applications [18–21], because of its high photosensitivity and low toxicity [20–23]. Actually, its applications in visible-light-driven organic synthesis have been recently explored [24–27], despite the fact that pure  $\text{In}_2\text{S}_3$  generally suffers from relatively low photocatalytic activity.

Similar to conventional heterogeneous catalysis, heterogeneous

photocatalysis in organic synthesis is a multistep process [428]. It comprises the fast generation, recombination and migration of the photo-induced electron-hole pairs, as well as the slow mass transfer and absorption/desorption of reactant/product molecules on the active surface. Therefore, the performance of a heterogeneous photocatalyst in the visible-light-driven organic synthesis is determined by all these steps. In order to improve the photocatalytic performances of  $\text{In}_2\text{S}_3$ , many efforts have been devoted. For example, co-catalysts can be loaded to suppress the recombination of the photo-induced electron-hole pairs and prolong the life of the charge carriers. To date,  $\text{In}_2\text{S}_3$ -based composites, with noble metals [29,30], graphene [26,31], carbon nanotubes [25], boron nitride [24] and semiconductors [19,32] as co-catalysts, have been developed to enhance the photocatalytic performance. On the other hand, the size and morphology of the photocatalysts have profound influence on not only the separation, migration and recombination of the photo-induced charge carriers, but also the mass transfer of reactants and active species [3334]. Therefore, many  $\text{In}_2\text{S}_3$ -based photocatalysts with various morphologies have been developed [202735]. Specially, hierarchical  $\text{In}_2\text{S}_3$ -based photocatalysts have shown improved performances, due to their hierarchical structures that increase the specific areas and facilitate the mass transfer [21,36,37]. Nevertheless, the hierarchical  $\text{In}_2\text{S}_3$  itself tend to be agglomerated, resulting in the shielding of light from irradiating, covering

\* Corresponding author.

E-mail address: [xiaobinfan@tju.edu.cn](mailto:xiaobinfan@tju.edu.cn) (X. Fan).

<https://doi.org/10.1016/j.apcatb.2018.05.087>

Received 22 February 2018; Received in revised form 22 May 2018; Accepted 29 May 2018  
Available online 30 May 2018

0926-3373/ © 2018 Elsevier B.V. All rights reserved.

the active sites on the catalyst surface, and increase in the mass transfer resistance.

Recently, two-dimensional materials have shown promising applications in photocatalysis. In particular, exfoliated Molybdenum disulfide ( $\text{MoS}_2$ ) or few layered  $\text{MoS}_2$  nanosheets, with a two-dimensional structure similar to graphene, are emerging photocatalytic co-catalysts [38–40]. The unique optical and electronic properties of  $\text{MoS}_2$  [41] can enhance the photoresponse and charge separation in the photocatalysts [42–44]. Some  $\text{In}_2\text{S}_3/\text{MoS}_2$  composites with enhanced photocatalytic  $\text{H}_2$  evolution rate [35,45] and excellent photoelectrochemical performance [46] have been investigated. It has been also found that  $\text{MoS}_2$  can activate  $\text{O}_2$ , facilitating the formation of superoxide radicals ( $\cdot\text{O}_2^-$ ) during the photo-oxidation [4447]. Since  $\cdot\text{O}_2^-$  plays a crucial role in numerous organic synthesis processes,  $\text{MoS}_2$  may have potential applications in photocatalytic organic synthesis. Especially, a two-dimensional hierarchical  $\text{In}_2\text{S}_3/\text{MoS}_2$  composite not only can reduce the agglomeration of  $\text{In}_2\text{S}_3$  and facilitate the charge separation, but also may have synergistic effect in many photoredox reactions.

To test this idea, we designed and constructed a two-dimensional hierarchical  $\text{In}_2\text{S}_3/\text{MoS}_2$  composite and investigated its photocatalytic performance in oxidative Aza-Henry reaction driven by visible light. Compared with pure  $\text{In}_2\text{S}_3$ , the photocatalytic activity of this hierarchical composite was remarkably enhanced. Moreover, it showed good stability and reusability with a decent performance in repeating experiments.

## 2. Experimental

### 2.1. Preparation of exfoliated $\text{MoS}_2$ nanosheets

The  $\text{MoS}_2$  nanosheets were fabricated using a chemical exfoliation method by lithium intercalation [48]. Typically, 1 g of bulk  $\text{MoS}_2$  powders and 10 ml *n*-butyl lithium (2.5 M in hexane) were added into a Schlenk flask under Ar atmosphere. Then, the mixture was ultrasonicated in a water bath at room temperature for 3 h. The intercalated samples were obtained by centrifugation and washed with hexane. The exfoliation was instantly carried out, with sonicating the fresh intercalated samples in water. After 30 min, the exfoliated  $\text{MoS}_2$  nanosheets were purified by centrifugation, washed three times with water, and completely dried by lyophilization.

### 2.2. Generation of $\text{In}_2\text{S}_3/\text{MoS}_2$ composite photocatalyst

In a typical procedure, a given mass of as-prepared  $\text{MoS}_2$  nanosheets were dispersed in 50 mL deionized water by ultrasonication. Subsequently, 0.5 mmol of  $\text{In}(\text{NO}_3)_3 \cdot 4.5\text{H}_2\text{O}$  was added into the  $\text{MoS}_2$  suspension. After stirring of 30 min, 2 mmol of L-cysteine was dissolved in the above mixture and stirred for another 30 min. Then, the pH of the obtained dispersion was adjusted to 8 by adding 1 M NaOH solution. The mixture was transferred into a 100 mL Teflon-lined stainless steel autoclave and held for 16 h at 180 °C. The obtained precipitates were collected by filtration, washed thoroughly with ethanol and water respectively, and dried under vacuum. The pure  $\text{In}_2\text{S}_3$  was prepared in the absence of  $\text{MoS}_2$  nanosheets.

### 2.3. General procedure for the Aza-Henry reaction

0.1 mmol *N*-aryl-tetrahydroisoquinoline and 10 mg  $\text{In}_2\text{S}_3/\text{MoS}_2$  composite were dispersed in 1 mL nitromethane by ultrasonication for 1 min. With an  $\text{O}_2$ -balloon providing an oxygen atmosphere, the mixture was stirring at room temperature for 24 h under the irradiation of a 20 W LED bulb (Fig. S1). Then, the catalyst was removed by filtration, and the filtrate was analyzed by gas chromatography (GC). The generated  $\text{H}_2\text{O}_2$  in the system was detected by a colorimetric method with copper (II) ions and DMP at 454 nm [47,49].

### 2.4. Photoelectrochemical (PEC) measurements

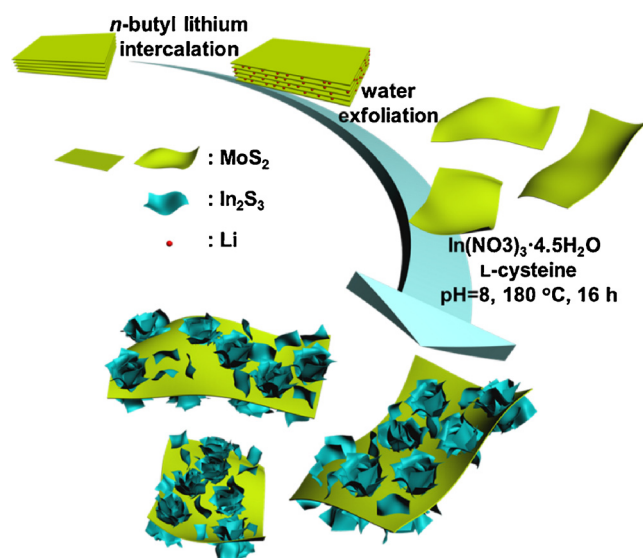
PEC characterization was conducted on an electrochemical analyzer (CHI660E Instruments), and a 300 W Xe lamp (Microsolar300, Perfectlight) with an AM 1.5 filter was employed as the light source. A Pt wire and Ag/AgCl electrode were used as the counter electrode and the reference electrode, respectively. The working electrode was fabricated as follows: 20 mg of the catalyst was added in a solution, which contained 0.8 mL of deionized (DI) water, 0.2 mL of ethanol, and 0.04 mL of 5 wt% Nafion solution. The as-prepared suspension was sonicated for 30 min to make a catalyst ink. Then, the ink was dropped onto an F-doped  $\text{SnO}_2$ -coated glass (FTO glass) with an active area of 1.0  $\text{cm}^2$ . The electrode was dried in the dark at 40 °C. Photocurrent response spectra were conducted in 0.2 M  $\text{Na}_2\text{SO}_4$  solution. The electrochemical impedance spectroscopy (EIS) was measured in the electrolyte of 0.1 M KCl aqueous solution with 2.5 mM  $\text{K}_3[\text{Fe}(\text{CN})_6]$ – $\text{K}_4[\text{Fe}(\text{CN})_6]$  (1 : 1) under open-circuit voltage.

### 2.5. Characterization

The samples were characterized by scanning electron microscopy (SEM; FEI Nanosem 430), transmission electron microscopy (TEM; JEM-2100 F), X-ray diffraction (XRD; AXS D8-Focus, Cu-K $\alpha$  radiation), Raman spectroscopy (Renishaw, inVia reflex), photoluminescence (PL) spectroscopy (Jobin Yvon, Fluorolog 3-21), UV–vis diffuse reflectance spectroscopy (UV-DRS; Shimadzu UV-2600) and  $\text{N}_2$  adsorption (Bjbuilder, SSA-7000). X-ray photoelectron spectroscopy (XPS) was performed in a PHI1600 spectrometer, and all the binding energies were referred to the C 1s peak of 284.8 eV. Electron spin resonance (ESR) spectra were measured by a Bruker EMXplus spectrometer. The photocatalytic results were measured by a gas chromatography (GC; Agilent 6890 N GC-FID system).  $^1\text{H}$  NMR results were recorded on a Bruker Avance III 400 MHz spectrometer in  $\text{CDCl}_3$  solution.

## 3. Results and discussion

The  $\text{In}_2\text{S}_3/\text{MoS}_2$  composite photocatalyst were fabricated as illustrated in Scheme 1. Firstly, the chemically exfoliated  $\text{MoS}_2$  nanosheets were prepared by a sonication-assisted intercalation process. Then,  $\text{In}_2\text{S}_3$  was grown *in situ* on the  $\text{MoS}_2$  nanosheets via a hydrothermal reaction. As shown in the powder X-ray diffraction (XRD) patterns (Fig. 1), similar diffraction peaks at 21.0°, 27.6°, 32.7° and 48.2° are obvious in both the  $\text{In}_2\text{S}_3$  and the composite, corresponding to the



Scheme 1. Illustration of the  $\text{In}_2\text{S}_3/\text{MoS}_2$  photocatalyst synthesis.

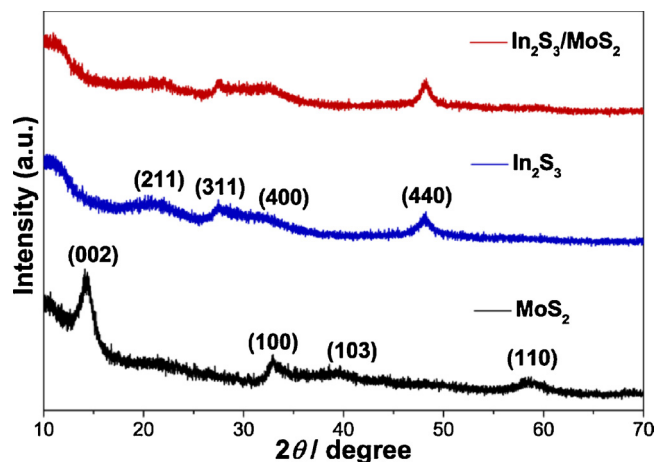


Fig. 1. XRD patterns of MoS<sub>2</sub> nanosheets, In<sub>2</sub>S<sub>3</sub> and In<sub>2</sub>S<sub>3</sub>/MoS<sub>2</sub> composite.

(211), (311), (400) and (440) of  $\beta$ -In<sub>2</sub>S<sub>3</sub> (JCPDS no. 32-0456), respectively [21,26]. Note that the disappearance of the characteristic (004) and (006), along with the presence of the (002), (100), (103), and (110) diffraction in the MoS<sub>2</sub> sample, indicate the exfoliated MoS<sub>2</sub> nanosheets are restacked, attributed to partial rotational ordering of the restacked dry phase [50]. However, combined with In<sub>2</sub>S<sub>3</sub>, these prominent peaks of MoS<sub>2</sub> completely disappear, suggesting the reduction of restacking, as well as the complete covering of the MoS<sub>2</sub> surfaces by the  $\beta$ -In<sub>2</sub>S<sub>3</sub> phase.

This assumption was supported by the morphology characterization with scanning electron microscopy (SEM). As shown in Fig. 2a–c, In<sub>2</sub>S<sub>3</sub> with the dahlia-flower-like structure are homogeneously grown on the both sides of two-dimensional MoS<sub>2</sub> nanosheets. Note that similar dahlia-flower-like In<sub>2</sub>S<sub>3</sub> grown in the control experiments without MoS<sub>2</sub> has a much larger diameter and tends to agglomerate randomly (Fig. S2). Besides, transmission electron microscopy (TEM) and corresponding quantitative energy dispersive X-ray spectroscopy (EDS) mapping reveal the overlapping distributions of elements In, Mo and S on the surface of composite (Fig. 2d–g, Fig. S3 and Table S1). In addition, as shown in the high-resolution TEM image of the composite

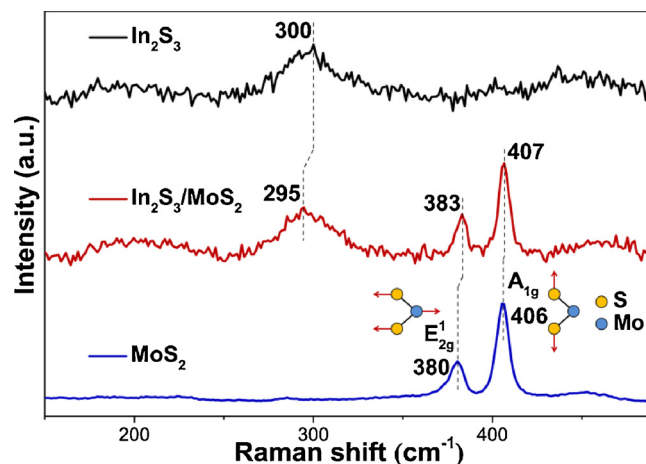


Fig. 3. Raman spectra of MoS<sub>2</sub> nanosheets, In<sub>2</sub>S<sub>3</sub> and the In<sub>2</sub>S<sub>3</sub>/MoS<sub>2</sub> composite.

(Fig. 2h), the lattice fringes with d-spacing of 0.27 and 0.32 nm can be assigned to the (100) of MoS<sub>2</sub> [51] and the (311) of In<sub>2</sub>S<sub>3</sub> [24], respectively. All these results confirm the successful growth of dahlia-flower-like In<sub>2</sub>S<sub>3</sub> on two-dimensional MoS<sub>2</sub> nanosheets. It should be noted that this interesting two-dimensional hierarchical structure could not only expose more surfaces and edges of In<sub>2</sub>S<sub>3</sub>, but should also facilitate the vectorial migration of photo-induced charge carriers between the In<sub>2</sub>S<sub>3</sub> and MoS<sub>2</sub>.

Raman spectroscopy is widely used to characterize the structural bonding nature in two-dimensional nanostructures like layered TMDs and related nanocomposites. As shown in Fig. 3, an obvious band appear at 300 cm<sup>-1</sup> for pure In<sub>2</sub>S<sub>3</sub>, corresponding to the typical mode of vibration in  $\beta$ -In<sub>2</sub>S<sub>3</sub> [46]. Notably, the band of In<sub>2</sub>S<sub>3</sub> downshifts from 300 to 295 cm<sup>-1</sup> in the composite. Presumably, the red shift may be attributed to the insertion of Mo<sup>4+</sup>. Considering that Mo<sup>4+</sup> radius is larger than that of the In<sup>3+</sup>, the bond force constant of Mo–S should be smaller, which may lead to the red shift of lattice vibration of the In<sub>2</sub>S<sub>3</sub> [46,52]. For the composite, another two major bands located at 383 and 407 cm<sup>-1</sup> can be assigned to the E<sub>2g</sub> and A<sub>1g</sub> modes of the present

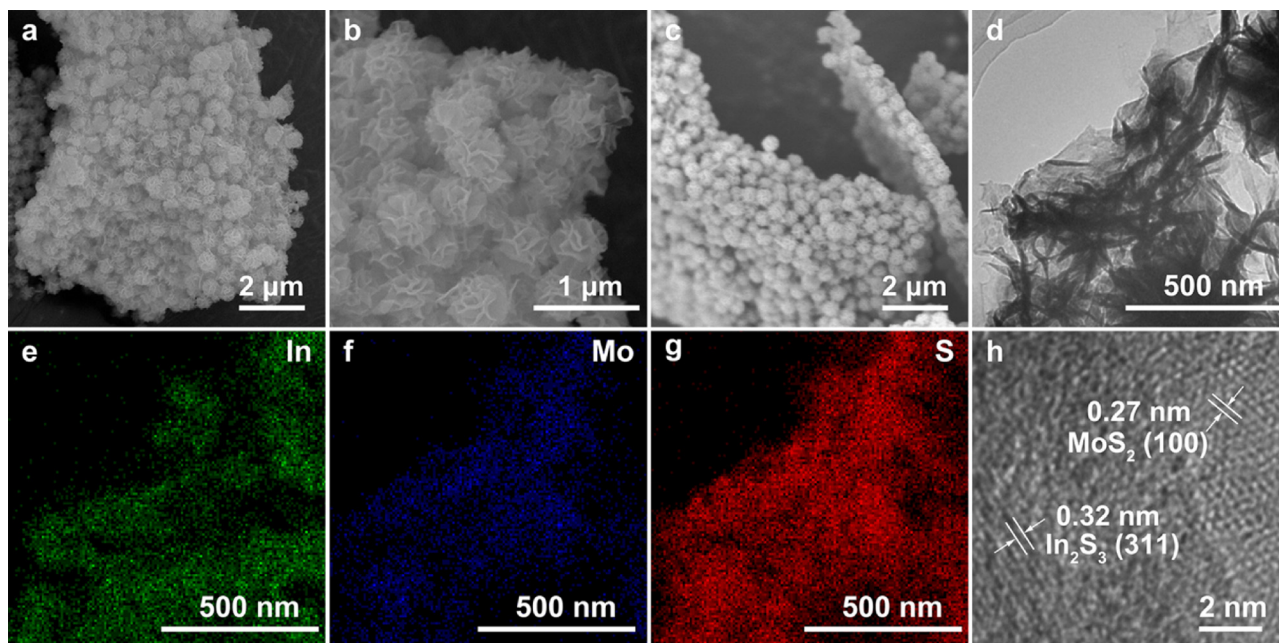


Fig. 2. (a–c) SEM images of In<sub>2</sub>S<sub>3</sub>/MoS<sub>2</sub> composite. (d) TEM image of In<sub>2</sub>S<sub>3</sub>/MoS<sub>2</sub> and corresponding quantitative EDS mapping of (e) In, (f) Mo and (g) S. (h) HRTEM image of In<sub>2</sub>S<sub>3</sub>/MoS<sub>2</sub>.



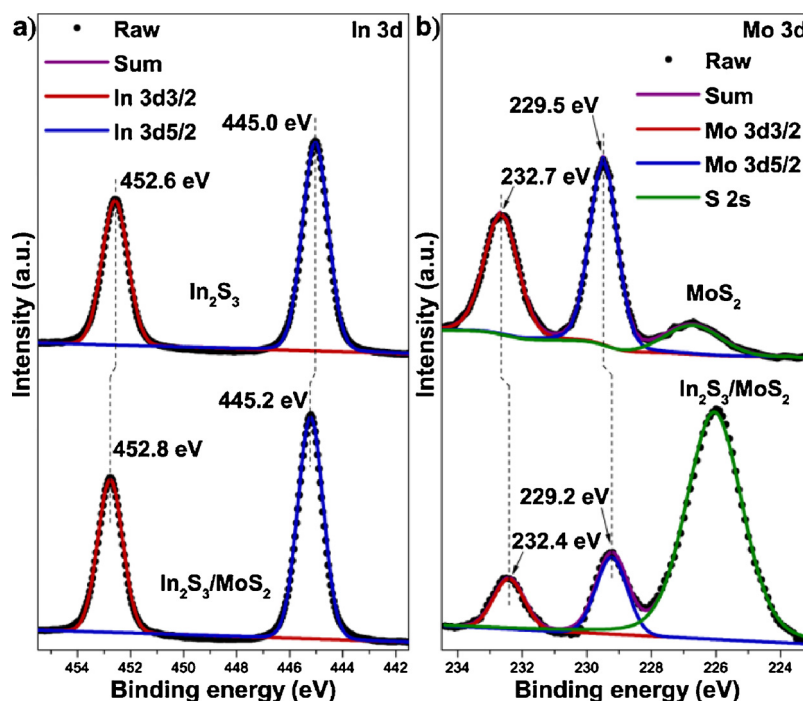


Fig. 4. (a) In 3d XPS spectra of  $\text{In}_2\text{S}_3$  and  $\text{In}_2\text{S}_3/\text{MoS}_2$  composite. (b) Mo 3d XPS spectra of  $\text{MoS}_2$  and  $\text{In}_2\text{S}_3/\text{MoS}_2$ .

$\text{MoS}_2$ , respectively [48]. It is worth noting that, compared with pure  $\text{MoS}_2$ , blueshifts of the  $E_{2g}^1$  and  $A_{1g}$  modes can be also observed. As known, the  $E_{2g}^1$  mode is associated with the in-plane opposite vibration of two S atoms with respect to the Mo atom, while the  $A_{1g}$  mode corresponding to the out-of-plane vibration of S atoms in opposite directions [53]. Both of them are highly sensitive to tensile or compressive strain, and variation of the local strain may give rise to the shifts of  $E_{2g}^1$  and  $A_{1g}$  band [54]. After combined with  $\text{In}_2\text{S}_3$ , the mismatch of the lattice spacing between  $\text{MoS}_2$  and  $\text{In}_2\text{S}_3$  may change the local strain on the surface of  $\text{MoS}_2$  nanosheets, causing the overall blueshifts of  $E_{2g}^1$  and  $A_{1g}$  band [4754]. The relatively larger blueshift ( $\sim 3 \text{ cm}^{-1}$ ) of the  $E_{2g}^1$  mode may be attributed to the covalent bonds between the In atoms and the S atoms on  $\text{MoS}_2$ , as the covalent bonds can suppress the in-plane vibration of the S atoms.

The interaction between the  $\text{In}_2\text{S}_3$  and  $\text{MoS}_2$  was further supported by X-ray photoelectron spectroscopy (XPS). As shown in Fig. 4a, in the spectrum for In 3d of pure  $\text{In}_2\text{S}_3$ , two peaks at 452.6 and 445.0 eV are assigned to In  $3d_{3/2}$  and In  $3d_{5/2}$ , indicating that In element exists in the chemical formation of  $\text{In}^{3+}$  [20]. Note that, after combined with  $\text{MoS}_2$ , the In  $3d_{3/2}$  and In  $3d_{5/2}$  slightly upshift to 452.8 and 445.2 eV, due to the decrease in the electronic density of  $\text{In}^{3+}$  [45,55]. Meanwhile, in pure  $\text{MoS}_2$ , Mo  $3d_{3/2}$  and Mo  $3d_{5/2}$  are located at 232.7 and 229.5 eV, demonstrating the existence of  $\text{Mo}^{4+}$ , and the peak corresponded to S 2s also appears (Fig. 4b) [48]. On the contrary, the binding energies of Mo  $3d_{3/2}$  and Mo  $3d_{5/2}$  for the composite are 0.3 eV lower than those of pure  $\text{MoS}_2$ , indicating that the electronic density of  $\text{Mo}^{4+}$  increases after combining with  $\text{In}_2\text{S}_3$  [55]. Besides, the increase of S 2s peak can be explained by the presence of  $\text{In}_2\text{S}_3$ . The change of the electronic density for  $\text{In}^{3+}$  and  $\text{Mo}^{4+}$  indicated the electrons are injected from  $\text{In}_2\text{S}_3$  to  $\text{MoS}_2$  [55]. Hence, it is suggested that the heterojunction is formed between  $\text{In}_2\text{S}_3$  and  $\text{MoS}_2$  during the hydrothermal synthesis process, and the photogenerated electrons on  $\text{In}_2\text{S}_3$  can transfer to  $\text{MoS}_2$ . This electrons transfer process can reduce the recombination possibility of electron-hole pairs on  $\text{In}_2\text{S}_3$  and enhance the photocatalytic activity of the composite, as demonstrated in the photoelectrochemical measurements as below.

Fig. 5a shows the transient photocurrent responses of pure  $\text{In}_2\text{S}_3$  and  $\text{In}_2\text{S}_3/\text{MoS}_2$  composite in the photoelectrochemical measurements,

which were carried out under intermittent visible light irradiation. Obviously, the photocurrent density of the composite is around 5.5-fold of that of the pure  $\text{In}_2\text{S}_3$ . As well known, the photocurrent is mainly generated by the diffusion of the photo-induced electrons to the back contact, with the photo-induced holes occupied by the hole acceptor in the electrolyte [56]. Hence, the superior photocurrent in the  $\text{In}_2\text{S}_3/\text{MoS}_2$  composite testifies that the photo-induced electron-hole pairs are more efficiently separated when compared with the pure  $\text{In}_2\text{S}_3$ .

To quantitatively evaluate their charge transfer resistance and the electrons life time, electrochemical impedance spectroscopy (EIS) was also carried out. As shown in Fig. 5b, the Nyquist arc radius of the composite is less than that of the pure  $\text{In}_2\text{S}_3$ , and the  $R_{ct}$  of the composite and pure  $\text{In}_2\text{S}_3$  are 11.3 and 75.6 k $\Omega$ , respectively. Note that a smaller  $R_{ct}$  (the interfacial electron transfer resistance) in the composite indicates the improved interfacial electron transfer [57]. Besides, corresponding Bode phase plots (Fig. 5c) reveals that the electron life time in the  $\text{In}_2\text{S}_3$  and the composite are 1.63 and 7.37 ms, respectively [58,59]. The prolonged electron life time in the composite should be attributed to the decrease in the recombination of the electron-hole pairs, as supported by the photoluminescence (PL) spectra (Fig. 5d). Generally, a higher PL intensity is accompanied by a higher recombination rate of the electron-hole pairs. Therefore, the obvious reduction of the PL intensity in the composite demonstrated that the combining  $\text{In}_2\text{S}_3$  with  $\text{MoS}_2$  could inhibit the electron-hole recombination [25]. Furthermore, the UV-vis diffuse reflectance spectra (DRS) show that the composite has enhanced absorption in the visible region, and its absorption edge downshifts to longer wavelength (Fig. 5e).

The Brunauer-Emmett-Teller (BET) analysis was also carried out to better understand the specific role of  $\text{MoS}_2$  nanosheets on the structural changes. As shown in Fig. 5f, both  $\text{In}_2\text{S}_3$  and the composite display the isotherms of type IV with a typical H3 hysteresis loop characteristic of mesoporous materials [27]. However, the surface area of the composite is 51.9  $\text{m}^2\text{g}^{-1}$ , which is much larger than that of pure  $\text{In}_2\text{S}_3$  (18.3  $\text{m}^2\text{g}^{-1}$ ). The increased surface area of the composite can be explained by its two-dimensional hierarchical structure, which can reduce the agglomeration of the flower-like  $\text{In}_2\text{S}_3$ . Generally, a larger surface area of the heterogenous photocatalyst can afford more active sites [26].

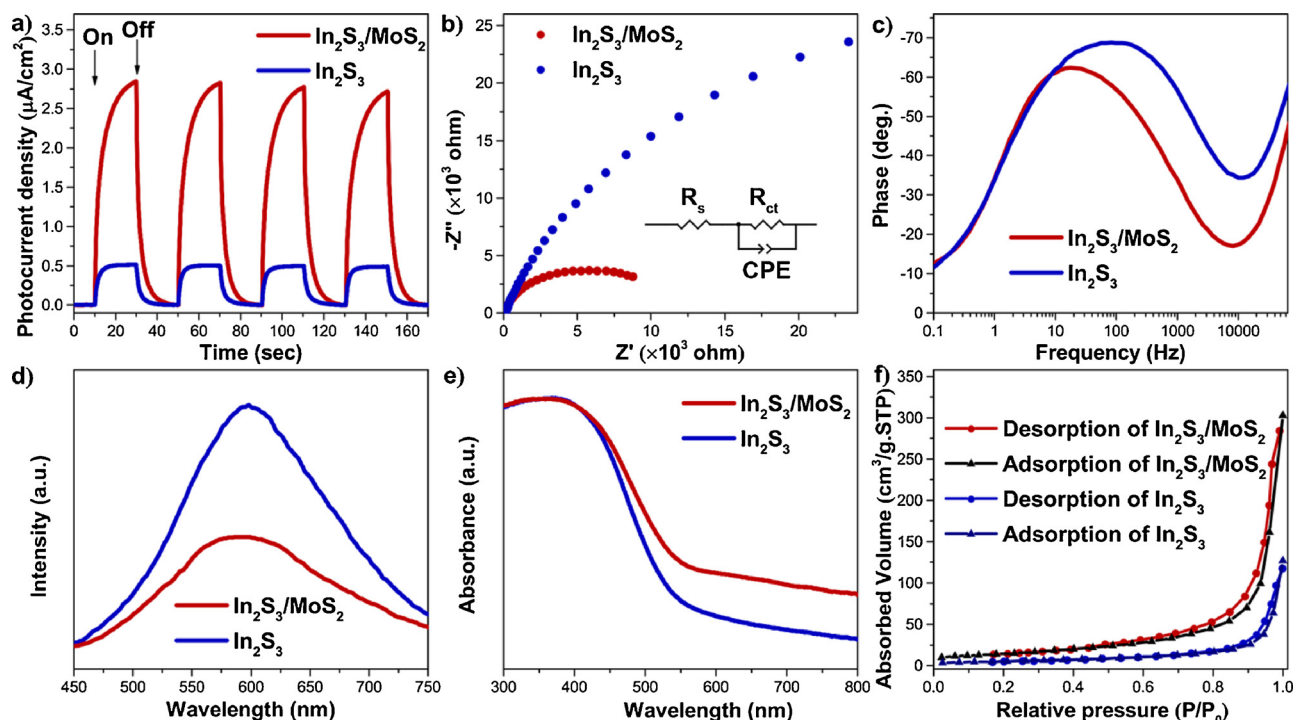


Fig. 5. (a) transient photocurrent density of  $\text{In}_2\text{S}_3$  and  $\text{In}_2\text{S}_3/\text{MoS}_2$ . (b) EIS Nyquist plots of  $\text{In}_2\text{S}_3$  and  $\text{In}_2\text{S}_3/\text{MoS}_2$ . (c) Bode phase plots of  $\text{In}_2\text{S}_3$  and  $\text{In}_2\text{S}_3/\text{MoS}_2$ . (d) Photoluminescence (PL) spectra of  $\text{In}_2\text{S}_3$  and  $\text{In}_2\text{S}_3/\text{MoS}_2$ . (e) UV-vis diffuse reflectance spectra (DRS) of pure  $\text{In}_2\text{S}_3$  and  $\text{In}_2\text{S}_3/\text{MoS}_2$ . (f) Nitrogen absorption-desorption isotherms of pure  $\text{In}_2\text{S}_3$  and  $\text{In}_2\text{S}_3/\text{MoS}_2$ .

Hence, enhanced photocatalytic performance of the composite could be also expected.

The photocatalytic activity of the samples was evaluated by the Aza-Henry reaction, which is an important C–C bond formation and one of the most exploited photocatalytic transformation [2,47]. *N*-aryl-tetrahydroisoquinoline (1a) was used as the amine substrate, and nitromethane was used as the solvent (Scheme 2). As shown in Fig. 6a, without catalyst or light, only negligible yields (3–4%) were observed for the desired product (2a). Meanwhile, the  $\text{MoS}_2$  alone showed a limited activity and selectivity (yield of 7%, and selectivity of 23%). However, repeated experiments demonstrated that the introduction of  $\text{MoS}_2$  could significantly improve the photocatalytic performance of  $\text{In}_2\text{S}_3$ . For example, the yield and selectivity of  $\text{In}_2\text{S}_3$  could increase from 48% and 60% to 74% and 77% in the  $\text{In}_2\text{S}_3/\text{MoS}_2$  composite (5 wt %), respectively. Note that further increase or decrease of the  $\text{MoS}_2$  content from 5 wt% would result in a degraded performance of the composite catalyst (Fig. 6b). The introduction of  $\text{MoS}_2$  could enhance the photocatalytic performance, due to the formation of the two-dimensional hierarchical heterojunction. However excess  $\text{MoS}_2$  might not efficiently form the  $\text{In}_2\text{S}_3/\text{MoS}_2$  heterojunction and inhibit the light irradiation on  $\text{In}_2\text{S}_3$ . Additionally, the active sites of the surface of  $\text{In}_2\text{S}_3$  might be covered by  $\text{MoS}_2$  [55,60]. Moreover, the  $\text{In}_2\text{S}_3/\text{MoS}_2$  composite showed excellent stability and reusability. As shown in Fig. 6c, the composite catalyst could be used for at least six times without obvious decline in its performances. XRD, FTIR and XPS tests of the recycled catalyst showed identical XRD, FTIR and XPS patterns of the

fresh counterpart, respectively (Fig. S5–8), and the morphology of the recycled catalyst did not display obvious change as seen in SEM image (Fig. S9), indicating the good stability of the composite. Although loading graphene or carbon nanotubes could slightly promote the photocatalytic activity of  $\text{In}_2\text{S}_3$ ,  $\text{In}_2\text{S}_3/\text{MoS}_2$  had superior performance to them, suggesting  $\text{MoS}_2$  might be a promising co-catalyst (Table S2). The influence of wavelength of the light source on the photocatalytic performance was investigated. The photocatalytic Aza-Henry reactions were carried out over  $\text{In}_2\text{S}_3/\text{MoS}_2$  composite, irradiated by LED bulbs with different wavelengths. The desired product was achieved using a blue (~470 nm) or green (~530 nm) LED bulb with an acceptable yield, whereas only limited yield was obtained under a red one (~630 nm) (Table S3). Red light, with a relatively long wavelength, could not effectively excite this  $\text{In}_2\text{S}_3$ -based photocatalyst, and photo-induced electron-hole pairs might be barely formed. Hence, the Aza-henry reaction was a wavelength-dependent photocatalytic process with  $\text{In}_2\text{S}_3/\text{MoS}_2$  composite as photocatalyst. The photocatalytic performances of the composite in the Aza-Henry reactions with different substrates were also investigated. As summarized in Table 1, we found that the  $\text{In}_2\text{S}_3/\text{MoS}_2$  composite is a universal photocatalyst for the Aza-Henry reaction.

To probe the mechanisms involved, the generated superoxide radicals ( $\cdot\text{O}_2^-$ ), hydroxyl radicals ( $\cdot\text{OH}$ ) and photo-generated holes ( $\text{h}^+$ ) were systematically investigated, as they are regarded as the major reactive species for the photocatalytic reaction. Benzoquinone (BQ), *tert*-butyl alcohol (TBA) and ammonium oxalate ( $\text{N}_2\text{H}_8\text{C}_2\text{O}_4$ , AO) were used as the scavengers for  $\cdot\text{O}_2^-$ ,  $\cdot\text{OH}$  and  $\text{h}^+$ , respectively [27,47]. Fig. 6d shows that the presence of either BQ or AO can significantly suppress the photocatalytic performance of  $\text{In}_2\text{S}_3$  and  $\text{In}_2\text{S}_3/\text{MoS}_2$ , suggesting that  $\cdot\text{O}_2^-$  and  $\text{h}^+$  are the main reactive species for the photocatalytic Aza-Henry reaction. Band positions analysis reveals that the valence band potential ( $E_{\text{VB}}$ ) and conduction band potential ( $E_{\text{CB}}$ ) of  $\text{In}_2\text{S}_3$  are about 1.25 and  $-0.85$  eV versus NHE, respectively. And the  $E_{\text{VB}}$  and  $E_{\text{CB}}$  of the  $\text{MoS}_2$  can be estimated to be 1.75 and  $-0.06$  eV versus NHE, respectively (Supplementary Data). Therefore, in addition



Scheme 2. Oxidative Aza-Henry reaction of *N*-aryl-tetrahydroisoquinoline with nitromethane.

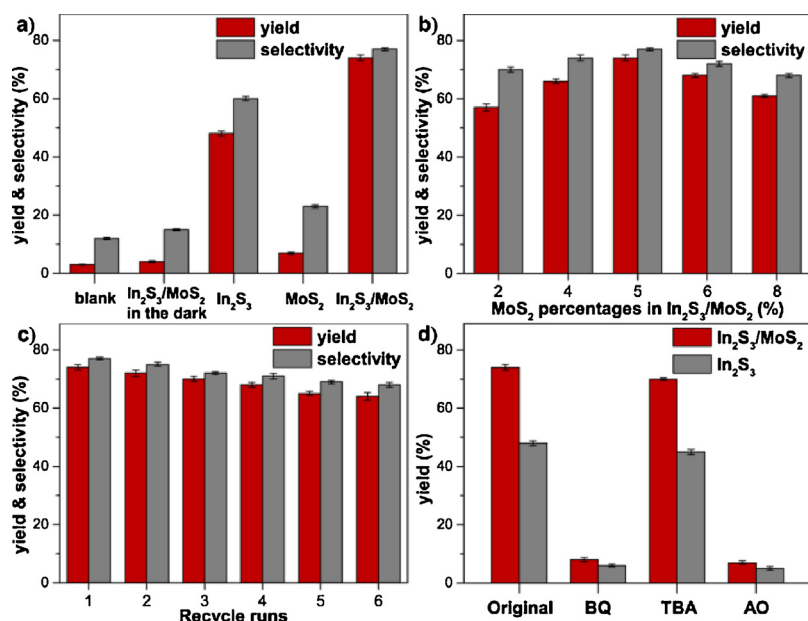


Fig. 6. (a) Oxidative Aza-Henry reaction of *N*-aryl-tetrahydroisoquinoline with nitromethane. (b) Photocatalytic oxidative Aza-Henry reaction by photocatalysts with different MoS<sub>2</sub> percentages. (c) Recyclability of In<sub>2</sub>S<sub>3</sub>/MoS<sub>2</sub> composite in photocatalytic oxidative Aza-Henry reaction. (d) Controlled experiments using different scavengers for the oxidative Aza-Henry reaction over In<sub>2</sub>S<sub>3</sub> and In<sub>2</sub>S<sub>3</sub>/MoS<sub>2</sub>.

Table 1

Substrate scope of the oxidative Aza-Henry reaction over In<sub>2</sub>S<sub>3</sub>/MoS<sub>2</sub> composite.<sup>a</sup>

Entry	Substrate	Product	Yield[%] <sup>b</sup>	Selectivity[%]
1	MeNO <sub>2</sub>		74	77
2	EtNO <sub>2</sub>		65 <sup>c</sup>	70
3			56 <sup>d</sup>	75
4			53	64
5			50	62
6 <sup>e</sup>	NC-CH <sub>2</sub> -CN		48	57

<sup>a</sup> Standard conditions: 1a (0.1 mmol) and catalyst were added in solvent (1 mL). The reaction was conducted in a Schlenk tube with an attached oxygen balloon and irradiated by a 20 W LED bulb for 24 h.

<sup>b</sup> Calibrated yields determined by GC.

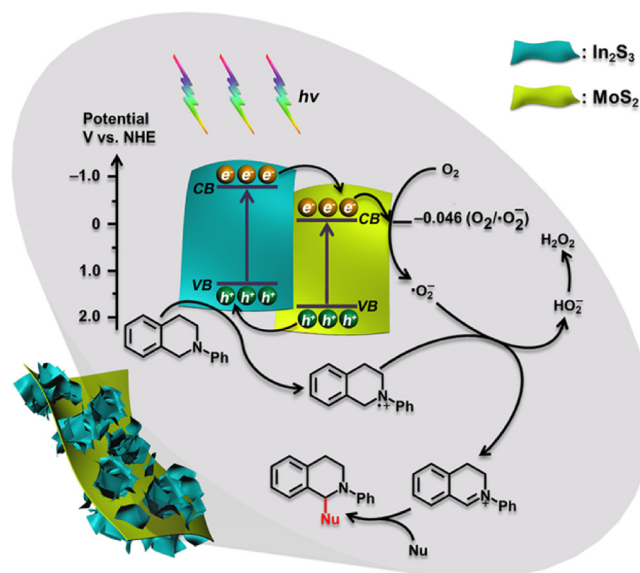
<sup>c</sup> dr = 2 : 1.

<sup>d</sup> dr = 1.5 : 1.

<sup>e</sup> The reaction was run with 1a (0.1 mmol), malononitrile (1.0 equiv) and catalyst in 1 mL DMF.

to the advantages of the two-dimensional hierarchical structure, the enhanced performances of the In<sub>2</sub>S<sub>3</sub>/MoS<sub>2</sub> composite can be explained by the In<sub>2</sub>S<sub>3</sub>/MoS<sub>2</sub> heterojunction that facilitates the generation and migration of the  $\cdot\text{O}_2^-$  and  $\text{h}^+$ .

As illustrated in Scheme 3, since the MoS<sub>2</sub> and In<sub>2</sub>S<sub>3</sub> have overlapping band potentials, they could form an effective heterojunction [61]. Under visible light illumination, the electrons were readily excited from valence band (VB) to conduction band (CB) in both MoS<sub>2</sub> and In<sub>2</sub>S<sub>3</sub>, generating the photo-induced electron-hole pairs. Then, the photogenerated electrons in In<sub>2</sub>S<sub>3</sub> could easily migrate to the MoS<sub>2</sub> surface, due to the more negative potential of CB in In<sub>2</sub>S<sub>3</sub>. Simultaneously, the holes generated in the VB of MoS<sub>2</sub> could migrate to In<sub>2</sub>S<sub>3</sub>.



Scheme 3. Proposed mechanism for oxidative Aza-Henry reaction photocatalyzed by In<sub>2</sub>S<sub>3</sub>/MoS<sub>2</sub> composite under visible light.

The transfer of electrons and holes in heterojunction could efficiently enhance the separation of photo-induced electron-hole pairs, suppress their recombination and prolong the life time. Additionally, the Mo atoms of the edges of MoS<sub>2</sub> might serve as preferred sites for absorption of O<sub>2</sub> [44,47], and the CB of MoS<sub>2</sub> possessed more negative potential than standard redox potential of O<sub>2</sub>/·O<sub>2</sub><sup>-</sup> (-0.046 eV vs. NHE) [62]. Therefore, the photogenerated electrons in MoS<sub>2</sub> could readily reduce O<sub>2</sub> to ·O<sub>2</sub><sup>-</sup>, which played a crucial role in the photocatalytic Aza-Henry reaction as mentioned above. That is, the ability of MoS<sub>2</sub> to activate O<sub>2</sub> enhanced the photocatalytic performance of catalysts [44,47]. Moreover, the superoxide radical anions in the In<sub>2</sub>S<sub>3</sub> and In<sub>2</sub>S<sub>3</sub>/MoS<sub>2</sub> system were measured by electron spin resonance (ESR) spectroscopy with 5,5-dimethyl-1-pyrroline-N-oxide (DMPO) as a probe. As shown in Fig. S2, no signal could be detected in the dark, whereas the DMPO-·O<sub>2</sub><sup>-</sup> species appeared in both samples after irradiation. Notably, compared with pure In<sub>2</sub>S<sub>3</sub>, In<sub>2</sub>S<sub>3</sub>/MoS<sub>2</sub> showed higher intensity of DMPO-·O<sub>2</sub><sup>-</sup>, indicating more superoxide radical anions were formed in the In<sub>2</sub>S<sub>3</sub>/MoS<sub>2</sub> system [47]. Hence, it was suggested that MoS<sub>2</sub> might activate O<sub>2</sub>,

facilitating the generation of  $\cdot\text{O}_2^-$ . On the other hand, an electron of tertiary amine could be abstracted by the photogenerated hole *via* a single electron transfer (SET) process, giving the tertiary amine radical cation [4,47]. Then, the cation bequeathed one hydrogen atom to the superoxide radical and formed an iminium ion. Nucleophiles can trap the iminium ion to release the final products.

The applicability of  $\text{In}_2\text{S}_3/\text{MoS}_2$  composite in other visible-light-driven reactions was also demonstrated. As shown in Scheme S1,  $\text{In}_2\text{S}_3/\text{MoS}_2$  composite could catalyze the selective aerobic oxidation of a series of primary amines to their corresponding imines [17]. Additionally, it could also be used as a photocatalyst in  $\alpha$ -arylation of bromomalonate *via* direct intermolecular C–H functionalization and oxyamination of 3-phenylpropanal [15]. Delightedly, the desired products had acceptable yields and selectivities, indicating the universality of  $\text{In}_2\text{S}_3/\text{MoS}_2$  composite in visible-light-driven organic synthesis.

#### 4. Conclusions

In summary, we successfully designed and fabricated the two-dimensional hierarchical  $\text{In}_2\text{S}_3/\text{MoS}_2$  composite by a simple method. This new composite catalyst displayed a remarkably enhanced photocatalytic performance in the Aza-Henry reaction compared with pure  $\text{In}_2\text{S}_3$ . In specific, the composite consisting of 95%  $\text{In}_2\text{S}_3$  and 5%  $\text{MoS}_2$  nanosheets showed the highest activity and selectivity. Systematical studies prove that the combination of the  $\text{In}_2\text{S}_3$  and  $\text{MoS}_2$  in such a two-dimensional hierarchical way can increase the light absorption in the visible region, facilitate the separation of the photo-induced electron–hole pairs, and provide more accessible active sites for the photoreaction. In addition, mechanism study reveals that the enhanced performances of the  $\text{In}_2\text{S}_3/\text{MoS}_2$  composite can be also explained by the formation of  $\text{In}_2\text{S}_3/\text{MoS}_2$  heterojunction that facilitates the generation and migration of the  $\cdot\text{O}_2^-$  and  $\text{h}^+$ .

#### Acknowledgment

This study was supported by the National Natural Science Funds (No. 21676198; No. 21403115) and the Program of Introducing Talents of Discipline to Universities (No. B06006).

#### Appendix A. Supplementary data

Supplementary material related to this article can be found, in the online version, at doi:<https://doi.org/10.1016/j.apcatb.2018.05.087>.

#### References

- H. Seo, M.H. Katcher, T.F. Jamison, *Nat. Chem.* 9 (2017) 453–456.
- N.A. Romero, D.A. Nicewicz, *Chem. Rev.* 116 (2016) 10075–10166.
- K. Mori, M. Kawashima, H. Yamashita, *Chem. Commun.* 50 (2014) 14501–14503.
- J. Wang, J. Ma, X. Li, Y. Li, G. Zhang, F. Zhang, X. Fan, *Chem. Commun.* 50 (2014) 14237–14240.
- J. Davies, T.D. Svejstrup, D. Fernandez Reina, N.S. Sheikh, D. Leonori, *J. Am. Chem. Soc.* 138 (2016) 8092–8095.
- S.P. Pitre, C.D. McTiernan, J.C. Scaiano, *Acc. Chem. Res.* 49 (2016) 1320–1330.
- E.B. Corcoran, M.T. Pirnot, S. Lin, S.D. Dreher, D.A. DiRocco, I.W. Davies, S.L. Buchwald, *D.W. MacMillan, Science* 353 (2016) 279–283.
- J. Xie, H. Jin, A.S.K. Hashmi, *Chem. Soc. Rev.* 46 (2017) 5193–5203.
- J.C. Chu, T. Rovis, *Nature* 539 (2016) 272–275.
- J.A. Caputo, L.C. Frenette, N. Zhao, K.L. Sowers, T.D. Krauss, D.J. Weix, *J. Am. Chem. Soc.* 139 (2017) 4250–4253.
- X. Li, J. Wang, D. Xu, Z. Sun, Q. Zhao, W. Peng, Y. Li, G. Zhang, F. Zhang, X. Fan, *ACS Sustain. Chem. Eng.* 3 (2015) 1017–1022.
- Z. Li, W.F. Zhang, Q.S. Zhao, H.Y. Gu, Y. Li, G.L. Zhang, F.B. Zhang, X.B. Fan, *ACS Sustain. Chem. Eng.* 3 (2015) 468–474.
- T. Kamegawa, S. Matsuura, H. Seto, H. Yamashita, *Angew. Chem. Int. Ed.* 52 (2013) 916–919.
- X. Qian, K. Fuku, Y. Kuwahara, T. Kamegawa, K. Mori, H. Yamashita, *ChemSusChem* 7 (2014) 1528–1536.
- Z. Xie, C. Wang, K.E. deKrafft, W. Lin, *J. Am. Chem. Soc.* 133 (2011) 2056–2059.
- J.-X. Jiang, Y. Li, X. Wu, J. Xiao, D.J. Adams, A.I. Cooper, *Macromolecules* 46 (2013) 8779–8783.
- C. Wang, Z. Xie, K.E. deKrafft, W. Lin, *J. Am. Chem. Soc.* 133 (2011) 13445–13454.
- Y. Li, G. Chen, Q. Wang, X. Wang, A. Zhou, Z. Shen, *Adv. Funct. Mater.* 20 (2010) 3390–3398.
- M. Dan, Q. Zhang, S. Yu, A. Prakash, Y. Lin, Y. Zhou, *Appl. Catal., B* 217 (2017) 530–539.
- W. Gao, W. Liu, Y. Leng, X. Wang, X. Wang, B. Hu, D. Yu, Y. Sang, H. Liu, *Appl. Catal., B* 176–177 (2015) 83–90.
- R. Wu, Y. Xu, R. Xu, Y. Huang, B. Zhang, *J. Mater. Chem. A* 3 (2015) 1930–1934.
- K.H. Park, K. Jang, S.U. Son, *Angew. Chem. Int. Ed.* 45 (2006) 4608–4612.
- Y. Tian, L. Wang, H. Tang, W. Zhou, *J. Mater. Chem. A* 3 (2015) 11294–11301.
- S. Meng, X. Ye, X. Ning, M. Xie, X. Fu, S. Chen, *Appl. Catal., B* 182 (2016) 356–368.
- M.-Q. Yang, B. Weng, Y.-J. Xu, *J. Mater. Chem. A* 2 (2014) 1710–1720.
- X. Li, B. Weng, N. Zhang, Y.-J. Xu, *RSC Adv.* 4 (2014) 64484–64493.
- M. Xie, X. Dai, S. Meng, X. Fu, S. Chen, *Chem. Eng. J.* 245 (2014) 107–116.
- J. Ran, J. Zhang, J. Yu, M. Jaroniec, S.Z. Qiao, *Chem. Soc. Rev.* 43 (2014) 7787–7812.
- T. Yan, J. Tian, W. Guan, Z. Qiao, W. Li, J. You, B. Huang, *Appl. Catal., B* 202 (2017) 84–94.
- F. Wang, Z. Jin, Y. Jiang, E.H.G. Backus, M. Bonn, S.N. Lou, D. Turchinovich, R. Amal, *Appl. Catal., B* 198 (2016) 25–31.
- X. An, J.C. Yu, F. Wang, C. Li, Y. Li, *Appl. Catal., B* 129 (2013) 80–88.
- S. Khanchandani, S. Kundu, A. Patra, A.K. Ganguli, *J. Phys. Chem. C* 117 (2013) 5558–5567.
- Y.F. Li, Z.P. Liu, *J. Am. Chem. Soc.* 133 (2011) 15743–15752.
- S. Yang, C.Y. Xu, B.Y. Zhang, L. Yang, S.P. Hu, L. Zhen, *J. Colloid. Interf. Sci.* 491 (2017) 230–237.
- W. Jiang, Y. Liu, R. Zong, Z. Li, W. Yao, Y. Zhu, *J. Mater. Chem. A* 3 (2015) 18406–18412.
- X. Zhang, X. Li, C. Shao, J. Li, M. Zhang, P. Zhang, K. Wang, N. Lu, Y. Liu, *J. Hazard. Mater.* 260 (2013) 892–900.
- S. Wang, B.Y. Guan, Y. Lu, X.W.D. Lou, *J. Am. Chem. Soc.* 139 (2017) 17305–17308.
- Y.-J. Yuan, Z.-J. Ye, H.-W. Lu, B. Hu, Y.-H. Li, D.-Q. Chen, J.-S. Zhong, Z.-T. Yu, Z.-G. Zou, *ACS Catal.* 6 (2015) 532–541.
- X. Fan, P. Xu, Y.C. Li, D. Zhou, Y. Sun, M.A. Nguyen, M. Terrones, T.E. Mallouk, *J. Am. Chem. Soc.* 138 (2016) 5143–5149.
- T.F. Jaramillo, K.P. Jorgensen, J. Bonde, J.H. Nielsen, S. Hørch, I. Chorkendorff, *Science* 317 (2007) 100–102.
- Q.H. Wang, K. Kalantar-Zadeh, A. Kis, J.N. Coleman, M.S. Strano, *Nat. Nanotechnol.* 7 (2012) 699–712.
- X.Y. Liu, H. Chen, R. Wang, Y. Shang, Q. Zhang, W. Li, G. Zhang, J. Su, C.T. Dinh, F.P.G. de Arquer, J. Li, J. Jiang, Q. Mi, R. Si, X. Li, Y. Sun, Y.T. Long, H. Tian, E.H. Sargent, Z. Ning, *Adv. Mater.* 29 (2017).
- K. Chang, X. Hai, J. Ye, *Adv. Energy Mater.* 6 (2016) 1502555.
- W.C. Peng, X. Wang, X.Y. Li, *Nanoscale* 6 (2014) 8311–8317.
- Z. Fang, X. Huang, Y. Wang, W. Peng, Y. Zhang, S. Weng, X. Fu, P. Liu, *J. Mater. Chem. A* 4 (2016) 13980–13988.
- F. Liu, Y. Jiang, J. Yang, M. Hao, Z. Tong, L. Jiang, Z. Wu, *Chem. Commun.* 52 (2016) 1867–1870.
- Z. Li, Y. Pi, D. Xu, Y. Li, W. Peng, G. Zhang, F. Zhang, X. Fan, *Appl. Catal., B* 213 (2017) 1–8.
- X. Fan, P. Xu, D. Zhou, Y. Sun, Y.C. Li, M.A. Nguyen, M. Terrones, T.E. Mallouk, *Nano Lett.* 15 (2015) 5956–5960.
- X. Zeng, Z. Wang, N. Meng, D.T. McCarthy, A. Deletic, J.-h. Pan, X. Zhang, *Appl. Catal., B* 202 (2017) 33–41.
- P. Joensen, E.D. Crozier, N. Alberding, R.F. Frindt, *J. Phys. C* 20 (1987) 4043.
- Z. Sun, Q. Zhao, G. Zhang, Y. Li, G. Zhang, F. Zhang, X. Fan, *RSC Adv.* 5 (2015) 10352–10357.
- Z. Tong, C. Yan, Z. Su, F. Zeng, J. Yang, Y. Li, L. Jiang, Y. Lai, F. Liu, *Appl. Phys. Lett.* 105 (2014) 223903.
- E. Parzinger, B. Miller, B. Blaschke, J.A. Garrido, J.W. Ager, A. Holleitner, U. Wurstbauer, *ACS Nano* 9 (2015) 11302–11309.
- L. Oakes, R. Carter, T. Hanken, A.P. Cohn, K. Share, B. Schmidt, C.L. Pint, *Nat. Commun.* 7 (2016) 11796.
- J. Xu, X. Cao, *Chem. Eng. J.* 260 (2015) 642–648.
- N. Zhang, Y. Zhang, X. Pan, X. Fu, S. Liu, Y.-J. Xu, *J. Phys. Chem. C* 115 (2011) 23501–23511.
- H.L. Guo, X.F. Wang, Q.Y. Qian, F.B. Wang, X.H. Xia, *ACS Nano* 3 (2009) 2653–2659.
- R. Kern, R. Sastrawan, J. Ferber, R. Stangl, J. Luther, *Electrochim. Acta* 47 (2002) 4213–4225.
- M. Zhou, J. Bao, Y. Xu, J. Zhang, J. Xie, M. Guan, C. Wang, L. Wen, Y. Lei, Y. Xie, *ACS Nano* 8 (2014) 7088–7098.
- N. Tian, Z. Li, D. Xu, Y. Li, W. Peng, G. Zhang, F. Zhang, X. Fan, *Ind. Eng. Chem. Res.* 55 (2016) 8726–8732.
- H. Wang, L. Zhang, Z. Chen, J. Hu, S. Li, Z. Wang, J. Liu, X. Wang, *Chem. Soc. Rev.* 43 (2014) 5234–5244.
- F. Zhang, X. Li, Q. Zhao, D. Zhang, *ACS Sustain. Chem. Eng.* 4 (2016) 4554–4562.